CHAPTER 2

INFORMATION TRANSFER ACROSS A GAP*

2.1. Overview

Faster communication between electronic devices inside a semiconductor chip may be enabled by optical interconnects based on surface-plasmon-polariton (SPP) waves, as their high localization overcomes the size mismatch between optical and electronic devices. Hence, time-domain Maxwell equations are solved to investigate the jump of a pulse-modulated carrier SPP wave across a semi-infinite gap on the metallic side of a planar metal/dielectric interface. The Drude model is used for the susceptibility of the metal and the air is taken as the dielectric material in our calculations. The Pearson correlation coefficient of the appropriate component of the Poynting vector at two points on either side of the gap is calculated. After an abrupt termination of the metal, reflection is very low and the signal continues to propagate in the air as a precursor followed by a somewhat distorted version of the launched pulse. Information encoded as the existence of a pulse is strongly and positively correlated with the transmitted signal. When the metal/air interface is restored after a gap of width equal to the carrier wavelength in free space, the signal received across the gap still comprises a precursor and a main pulse that are still strongly and positively correlated with the transmitted signal. Thus, information continues to propagate in the forward direction for a long distance after the gap, a

promising result for SPP-wave-based optical interconnects.

2.2. Introduction

Faster communication between electronic devices inside a semiconductor chip is currently limited by unacceptably high increase of temperature. A higher data-transfer rate would require a higher pulse repetition frequency, which would result in more dissipation of thermal energy in electronic interconnects. Furthermore, a higher device density would require electronic interconnects to be of smaller cross-section, but that would increase the resistance of the interconnect to increase the time taken by a pulse to travel through an interconnect of fixed length. Conventional optical interconnects are faster, but their large sizes ($\gtrsim 500\,\mathrm{nm}$) make it difficult to integrate them with dense arrays of the much smaller electronic devices (10–50 nm). As the electromagnetic fields of SPP waves are highly localized to dielectric/metal interfaces, SPP-wave-based optical interconnects hold promise [Ozbay (2006), Sekhon and Verma (2011)].

Plasmonics research has come a long way from the late 1940s when certain electronic phenomena in metals exposed to electric fields were resolved in terms of plasma oscillations [Bohm and Gross (1949)a, Bohm and Gross (1949)b]. The quantum of plasma oscillations was dubbed the plasmon [Pines (1956)]. A few years later, the energy losses of electrons impinging on a metal film were explained in terms of electronic-plasma oscillations occurring at the film's surfaces [Ritchie (1957)], the quantum of these oscillations being called the surface plasmon. When the vacuum is replaced by a dielectric material, the quantum is called a surface-plasmon-polariton, with a plasmonic component in the metal and a polaritonic component in the dielectric material. SPP waves are classical counterparts of SPP trains [Maier (2007), Polo *et al.* (2013)].

Theoretical [Turbadar (1959)] and experimental [Otto (1968), Kretschmann and Raether (1968)] frequency-domain developments within a decade made the optical excitation of SPP waves a very easy task even for undergraduate students [Simon *et al.* (1975)]. The amplitude of an SPP wave is minuscule after a certain distance on either side of the metal/dielectric interface. This localization is a desirable quality for optical sensing, as was soon realized [Nylander *et al.* (1982)] and it continues to be exploited for very sensitive chemical sensors and biochemical sensors [Homola (2006), Abdulhalim *et al.* (2008)].

The same localization holds promise for thin optical interconnects in semiconductor chips [Ozbay (2006), Sekhon and Verma (2011)]. Although SPP-wave propagation along continuous planar dielectric/metal interfaces is heavily investigated using the Maxwell equations in the frequency domain [Maier (2007), Polo *et al.* (2013), Homola (2006), Abdulhalim *et al.* (2008)], the scattering of SPP waves by discontinuities is in an embryonic stage at best [Novitsky (2010), Foley *et al.* (2014)]. Such investigations must be done in the time domain, not the frequency domain, in order to avoid the Gibbs phenomenon [Körner (1988)]. A shift to the time domain would also facilitate investigation of information transmission by a carrier SPP wave across a discontinuity. Yet, that key requirement for the successful integration of surface-plasmonic communication with electronic devices [Barnes *et al.* (2003)] had remained unexplored, before this research was undertaken.

With this motivation, the scattering of a pulse-modulated SPP wave guided by a dielectric/metal interface by an infinitely deep gap in the metal is simulated. The finite-difference time-domain (FDTD) method [Yee (1966), Elsherbeni and Demir (2016)] is used to compute the temporal evolution of the electromagnetic fields everywhere in a computational domain encompassing the guiding interface as well as the gap. The fields

on the dielectric side of the interface are computed at two points on either side of the gap. The signal on the reception point after the gap is compared with the signal on the transmission point before the gap using the Pearson correlation coefficient [Rodgers and Nicewander (1988)]. As all calculations are performed in the time domain rather in the frequency domain, restrictions [Novitsky (2010)] on the constitutive properties of the dielectric material as well as doubtful extensions [Foley et al. (2014)] of Ibn Sahl's law of refraction [Rashed (1990)] are completely avoided.

The plan of this chapter is as follows: In Sec. 2.3., the initial-boundary-value problem for information transmission by a pulse-modulated SPP wave across an infinitely deep gap in the metal is formulated. The constitutive relations of the materials involved and the updating equations to implement the FDTD method are also provided in this section. Numerical results are presented and discussed in Sec. 2.4. The chapter concludes with some closing remarks in Sec. 2.5.
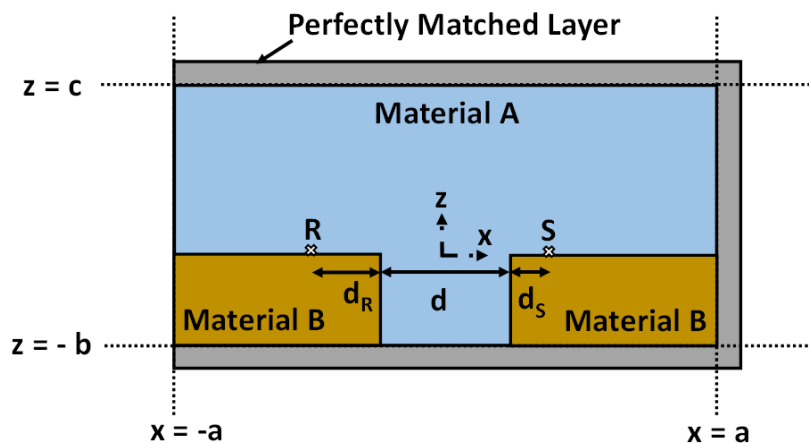
2.3.   Theoretical Analysis

Figure 2.1: Schematic of the computational domain of the initial boundary value problem solved for the information carried by a pulse-modulated SPP wave across a gap.

2.3.1. Initial-Boundary-Value Problem

Consider the computational domain of the initial-boundary-value problem depicted in Fig. 2.1. Whereas the relevant physical domain is identified by the region $\Re : \{|x| \leq a, -\infty < y < \infty, -b \leq z \leq c\}$ the relevant temporal domain is identified as $T : \{t \geq 0\}$. Thus, $\Re \times T$ is the computational domain. The region $\Re_A = \Re_A^{top} \cup \Re_A^{bot}$ is occupied by a homogeneous dielectric material labeled A, where $\Re_A^{top} : \{|x| \leq a, -\infty < y < \infty, 0 < z \leq c\}$ and $\Re_A^{bot} : \{|x| < d/2, -\infty < y < \infty, -b \leq z < 0\}$. The region $\Re_B = \Re_B^{left} \cup \Re_B^{right}$ is occupied by a homogeneous metal labeled B, where $\Re_B^{left} : \{-a \leq x < -d/2, -\infty < y < \infty, -b \leq z < 0\}$ and $\Re_B^{right} : \{d/2 < x \leq a, -\infty < y < \infty, -b \leq z < 0\}$. The materials A and B are to be chosen such that an SPP wave can travel guided by the plane $z = 0$ at a fixed frequency $f_c = \omega_c / 2\pi$, except that it is scattered by the gap $\Re_A^{bot}$ between $\Re_B^{left}$ and $\Re_B^{right}$. Above the plane $z = c$ and below the plane $z = -b$, perfectly matched layers (PMLs) [Berenger (1994)] bound $\Re_A$ to prevent reflections into $\Re$, even though the dimensions b and c must be chosen to be sufficiently large that the reflections are minuscule. As material B is a metal, b should exceed the skin depth [Iskander (2013)] at the carrier frequency f_c. All fields are independent of y, for which reason that coordinate is omitted from the balance of this chapter.

To analyze the adequacy of information transmission across the gap $\Re_A^{bot}$, a point labeled R ($x_R = -d_R - d/2$, $z_R = 0^+$) is identified as the point of transmission and a point labeled S ($x_S = d_S + d/2$, $z_S = 0^+$) as the point of reception, as shown in Fig.2.1.

The electromagnetic fields are specified by the following boundary conditions:

(i)   For, $x = -a$, $z \in (0, \infty)$,   and $t \in T$,   both $\mathbf{E}(x, z, t) = \mathbf{E}_A(z, t)$ and $\mathbf{H}(x, z, t) = \mathbf{H}_A(z, t)$ are known.

(ii)   For, $x = -a$, $z \in (-\infty, 0)$,   and $t \in T$,   both $\mathbf{E}(x,z,t) = \mathbf{E}_B(z,t)$ and

$\mathbf{H}(x,z,t) = \mathbf{H}_B(z,t)$ are known.

In addition to the boundary conditions (i) and (ii), the following initial condition is prescribed:

For, $x = -a$, $z \in (-\infty, \infty)$, and $t = 0$, both $\mathbf{E}(x,z,t) = 0$ and $\mathbf{H}(x,z,t) = 0$.

2.3.2. Constitutive Relations

As both materials A and B are chosen to be nonmagnetic, the time-domain constitutive relation

$$\mathbf{H}(x,z,t) = \mu_0^{-1}\mathbf{B}(x,z,t),\qquad(2.1)$$

applies everywhere in $\mathfrak{R}$ for all time in T, with μ_o as the permeability of free space (i.e., vacuum). Furthermore the time-domain constitutive relation

$$\mathbf{D}(x,z,t) = \begin{cases} \varepsilon_o\left(\varepsilon_A \star \mathbf{E}\right)(x,z,t), & (x,z) \in \mathfrak{R}_A, \\ \varepsilon_o\left(\varepsilon_B \star \mathbf{E}\right)(x,z,t), & (x,z) \in \mathfrak{R}_B, \end{cases}\qquad(2.2)$$

applies for all $t \in T$, with ε_o as the permittivity of free space; $\varepsilon_\ell(t)$, $\ell \in \{A,B\}$, as the time-domain relative permittivity function; and the convolution operation defined by

$$\left(\varepsilon_\ell \star \mathbf{E}\right)(x,z,t) \equiv \int_0^\infty \varepsilon_\ell(\tau)\mathbf{E}(x,z,t-\tau)d\tau, \quad \ell \in \{A,B\}.\qquad(2.3)$$

The presence of the convolution operator $\star$ in the constitutive relations reflects the dispersive nature of both materials. Let $\varepsilon_A(t)$ obey the Lorentz model [Kittel (1974)] of a dielectric material so that

$$\varepsilon_A(t) = \delta(t) + p_A\Omega_A \exp\left(-\frac{\Omega_A t}{2\pi N_A}\right)\sin\left(\Omega_A t\right)U(t),\qquad(2.4)$$

where the constants $\{p_A, \Omega_A, N_A\}$ quantify the oscillator strength as well as the resonance wavelength and linewidth of material A, $\delta(t)$ is the Dirac delta, and

$$U(t) = \begin{cases} 0, & t < 0, \\ 1, & t \geq 0, \end{cases} \tag{2.5}$$

is the unit step function. Let $\varepsilon_B(t)$ obey the Drude model [Johnson and Christy (1972), Yang *et al.* (2015)] of a metal; hence,

$$\varepsilon_B(t) = \delta(t) + \omega_B^2 \tau_B \left[1 - \exp\left(-\frac{t}{\tau_B} \right) \right] U(t), \tag{2.6}$$

where ω_B and τ_B are the plasma angular frequency and relaxation time, respectively.

The susceptibility function

$$\chi_\ell(t) = \varepsilon_\ell(t) - \delta(t), \quad \ell \in \{A, B\}, \tag{2.7}$$

is defined for later use, but note here $\chi_\ell(t) \equiv 0$ for $t \leq 0$ by virtue of the principle of causality [Hu (1989), Mackey and Lakhtakia (2010)]. After defining the Fourier transform [Körner (1988)]

$$\tilde{F}(\omega) = \int_{-\infty}^{\infty} F(t) \exp(i\omega t) dt, \tag{2.8}$$

where $i = \sqrt{-1}$, $\omega = 2\pi f$ is the angular frequency, and f is the frequency, one gets

$$\tilde{\chi}_\ell(\omega) = \tilde{\varepsilon}_\ell(\omega) - 1, \quad \ell \in \{A, B\}, \tag{2.9}$$

with

$$\tilde{\chi}_A(\omega) = \left\{ \frac{p_A \Omega_A}{\Omega_A^2 \left[1 + \left(2\pi N_A \right)^{-2} \right] - \omega^2 - i\omega\Omega_A / \pi N_A} \right\} \tag{2.10}$$

and

$$\tilde{\chi}_B(\omega) = -\left[\frac{\omega_B^2}{\omega\left(\omega + i / \tau_B \right)} \right]. \tag{2.11}$$

2.3.3. Initial Fields

The initial field at the boundary $x = -a$ arises from a pulse-modulated surface wave of frequency f_c , with the corresponding angular frequency $\omega_c = 2\pi f_c$ and the free-space wavenumber $k_c = \omega_c \sqrt{\varepsilon_o \mu_o}$. For the carrier surface wave to be an SPP wave, $\mathrm{Re}\left[\tilde{\varepsilon}_A(\omega_c)\right] > 1$, $\mathrm{Im}\left[\tilde{\varepsilon}_A(\omega_c)\right] \geq 0$, $\mathrm{Re}\left[\tilde{\varepsilon}_B(\omega_c)\right] < 0$, and $\mathrm{Im}\left[\tilde{\varepsilon}_B(\omega_c)\right] > 0$. Then,

$$\mathbf{E}_A(z,t) = g(t)\mathbf{Re}\left[\mathbf{E}_A(-a,z)\exp\left(-i\omega_c t\right)\right], \tag{2.12}$$

$$\mathbf{H}_A(z,t) = \mathbf{Re}\left[h(t)\mathbf{H}_A(-a,z)\exp\left(-i\omega_c t\right)\right], \tag{2.13}$$

$$\mathbf{E}_B(z,t) = g(t)\mathbf{Re}\left[\mathbf{E}_B(-a,z)\exp\left(-i\omega_c t\right)\right], \tag{2.14}$$

$$\mathbf{H}_B(z,t) = \mathbf{Re}\left[h(t)\mathbf{H}_B(-a,z)\exp\left(-i\omega_c t\right)\right], \tag{2.15}$$

where [Maier (2007), Polo *et al.* (2013)]

$$\mathbf{E}_A(x,z) = \left[\frac{-\alpha_{c_A}\,\hat{\mathbf{u}}_x + q_c\,\hat{\mathbf{u}}_z}{k_c\,\tilde{n}_A^2(\omega_c)}\right]\exp\left[i\left(q_c x + \alpha_{c_A} z\right)\right], \tag{2.16}$$

$$\mathbf{H}_A(x,z) = -\frac{1}{\eta_0}\,\hat{\mathbf{u}}_y\,\exp\left[i\left(q_c x + \alpha_{c_A} z\right)\right], \tag{2.17}$$

$$\mathbf{E}_B(x,z) = \left[\frac{-\alpha_{c_B}\,\hat{\mathbf{u}}_x + q_c\,\hat{\mathbf{u}}_z}{k_c\,\tilde{n}_B^2(\omega_c)}\right]\exp\left[i\left(q_c x - \alpha_{c_B} z\right)\right], \tag{2.18}$$

$$\mathbf{H}_B(x,z) = -\frac{1}{\eta_0}\,\hat{\mathbf{u}}_y\,\exp\left[i\left(q_c x + \alpha_{c_B} z\right)\right]. \tag{2.19}$$

In the foregoing equations, $\eta_0 = \sqrt{\mu_0/\varepsilon_0}$ is the intrinsic impedance of free space;

$$\alpha_{c_\ell} = \sqrt{k_c^2 \tilde{\varepsilon}_\ell(\omega_c) - q_c^2}, \quad \ell \in \{A, B\}, \tag{2.20}$$

is a complex wavenumber describing field variation along the z axis;

$$\tilde{n}_\ell(\omega) = \sqrt{\tilde{\varepsilon}_\ell(\omega)}, \quad \ell \in \{A, B\}, \tag{2.21}$$

is the complex refractive index; and

$$q_c = k_c \sqrt{\frac{\tilde{\varepsilon}_A(\omega_c)\tilde{\varepsilon}_B(\omega_c)}{\tilde{\varepsilon}_A(\omega_c) + \tilde{\varepsilon}_B(\omega_c)}} \qquad (2.22)$$

is the SPP wavenumber. The conditions $\text{Re}(q_c)\text{Im}(q_c) > 0$ and $\text{Im}(\alpha_{c_\ell}) > 0$, $\ell \in \{A, B\}$, apply. Finally, the magnitude of $\tilde{\mathbf{H}}_A(0,0^+) = \tilde{\mathbf{H}}_B(0,0^-)$ is fixed independent of ω_c in order to facilitate comparison of pulses carried by SPP waves of different angular frequencies.

The propagation distance along the x axis of the carrier SPP wave is $\Delta_{prop} = 1/\text{Im}(q_c)$, its phase speed is $v_p = \omega_c/\text{Re}(q_c)$, its depth of penetration in material A is $\Delta_A = 1/\text{Im}(\alpha_{c_A})$, and its depth of penetration in material B is $\Delta_B = 1/\text{Im}(\alpha_{c_B})$. The dimensions a, b, and c must be chosen to keep Δ_{prop}, Δ_A, and Δ_B in mind.

For all numerical results reported in Section 2.4, the pulse function is taken to be [Geddes III *et al.* (2000)]

$$g(t) = \omega_c t \exp(-\omega_c t) \qquad (2.23)$$

so that

$$h(t) = \left(\frac{1+i}{2}\right) g(t) + \frac{1}{2}\exp(-\omega_c t). \qquad (2.24)$$

2.3.4. FDTD Updating Equations

The FDTD updating equations can be obtained from the source-free Maxwell curl equations, i.e.,

$$\left. \begin{array}{l} \nabla \times \mathbf{E}(x,z,t) = -\partial_t \mathbf{B}(x,z,t) \\ \nabla \times \mathbf{H}(x,z,t) = \partial_t \mathbf{D}(x,z,t) \end{array} \right\}, \qquad (2.25)$$

where $\partial_w \equiv \partial/\partial w$. Since there is no variation with respect to y, $\partial_y \equiv 0$ and $\nabla \equiv \hat{\mathbf{u}}_x \partial_x + \hat{\mathbf{u}}_z \partial_z$.

On substituting Eqs. (2.1) and (2.2) in (2.25), two different autonomous systems of equations emerge. The first involves only the Cartesian components $E_x(x,z,t)$, $E_z(x,z,t)$, and $H_y(x,z,t)$; the second $E_y(x,z,t)$, $H_x(x,z,t)$, and $H_z(x,z,t)$. A quick glance at Sec. 2.3.3 suffices to indicate that only the first system needs to be solved for the present problem. Thus, the relevant equations applicable in $\Re_\ell$, $\ell \in \{A,B\}$, and T are as follows:

$$\left. \begin{array}{l} \varepsilon_0 \partial_t E_x(x,z,t) + \varepsilon_0 \partial_t \left[(\chi_\ell \star E_x)(x,z,t) \right] = -\partial_z H_y(x,z,t) \\ \varepsilon_0 \partial_t E_z(x,z,t) + \varepsilon_0 \partial_t \left[(\chi_\ell \star E_z)(x,z,t) \right] = \partial_x H_y(x,z,t) \\ \mu_0 \partial_t H_y(x,z,t) = \partial_x E_z(x,z,t) - \partial_z E_x(x,z,t) \end{array} \right\}. \tag{2.26}$$

The FDTD method requires the partitioning of

- $\Re$ into rectangular cells of dimension Δx along the x axis and Δz along the z axis, and

- T into linear cells of duration Δt.

For the stability of the FDTD method, we must choose Δt such that the Courant-Friedrichs-Lewy criterion [Elsherbeni and Demir (2016)]

$$c_0 \Delta t \sqrt{\left(\frac{1}{\Delta x} \right)^2 + \left(\frac{1}{\Delta z} \right)^2} \leq 1 \tag{2.27}$$

is satisfied, c_0 being the speed of light in free space.

Indexes m, n, and p are attached to discrete values of x, z, and t, respectively. Then, after defining

$$\chi^p(m,n) = \begin{cases} \chi_A(p\Delta t), & m\Delta x\, \hat{\mathbf{u}}_x + n\Delta z\, \hat{\mathbf{u}}_z \in R_A, \\ \chi_B(p\Delta t), & m\Delta x\, \hat{\mathbf{u}}_x + n\Delta z\, \hat{\mathbf{u}}_z \in R_B, \end{cases} \tag{2.28}$$

the   samples $E_x^p(m,n) = E_x(m\Delta x, n\Delta z, p\Delta t)$, $E_z^p(m,n) = E_z(m\Delta x, n\Delta z, p\Delta t)$,   and

$H_y^{p+\frac{1}{2}}(m,n) = H_y(m\Delta x, n\Delta z, \left(p+\dfrac{1}{2}\right)\Delta t)$ have to be determined from finite-difference

equations obtained by applying the central-difference formula [Geddes *et al.* (2000)] to

Eqs. 2.26. The relevant equations are as follows:

$$
\begin{aligned}
E_x^{p+1}(m,n) = {}& E_x^p(m,n) - \chi^p(m,n) E_x^1(m,n)\Delta t \\
& - \frac{\Delta t}{\varepsilon_0 \Delta z}\left[H_y^{p+\frac{1}{2}}(m,n) - H_y^{p+\frac{1}{2}}(m,n-1) \right] \\
& - \Delta t \sum_{\kappa=1}^{p-1}\left[\chi^\kappa(m,n)\left\{ E_x^{p-\kappa+1}(m,n) - E_x^{p-\kappa}(m,n) \right\} \right],
\end{aligned}
\tag{2.29}
$$

$$
\begin{aligned}
E_z^{p+1}(m,n) = {}& E_z^p(m,n) - \chi^p(m,n) E_z^1(m,n)\Delta t \\
& - \Delta t \sum_{\kappa=1}^{p-1}\left[\chi^\kappa(m,n)\left\{ E_z^{p-\kappa+1}(m,n) - E_z^{p-\kappa}(m,n) \right\} \right] \\
& + \frac{\Delta t}{\varepsilon_0 \Delta x}\left[H_y^{p+\frac{1}{2}}(m,n) - H_y^{p+\frac{1}{2}}(m-1,n) \right]
\end{aligned}
\tag{2.30}
$$

and

$$
\begin{aligned}
H_y^{p+\frac{1}{2}}(m,n) = {}& H_y^{p-\frac{1}{2}}(m,n) + \frac{\Delta t}{\mu_0 \Delta x}\left[E_z^p(m+1,n) - E_z^p(m,n) \right] \\
& - \frac{\Delta t}{\mu_0 \Delta z}\left[E_x^p(m,n+1) - E_x^p(m,n) \right]
\end{aligned}
\tag{2.31}
$$

Equations (2.29)-(2.31) give values of both non-zero components of the electric field and

the sole non-zero component of the magnetic field one time step into the future, based on

their values one time step in the past. Updating of the electric field is staggered with the

updating of the magnetic field as discussed in Sec. 1.5.

As shown in Fig.2.1, the computational domain $\mathfrak{R}$ is bounded by three PMLs so

as the prevent reflections back into the computational domain. Details of the incorporation

of the PML region comprising all three PMLs in the FDTD method are provided in

Appendix A and the MATLAB programs to obtain the numerical results are given in Appendix B.

2.4. Numerical Results and Discussion

For all numerical results presented here, material A is chosen to be air and approximated as vacuum by setting $p_A = 0$. Material B is chosen to be bulk silver with $\omega_B = 1.352 \times 10^{16}$ rad s^{-1} and $\tau_B = 17 \times 10^{-15}$ s [Yang *et al.* (2015)]. The computational domain $\Re$ with $a = 30000$ nm, $b = 4\Delta_B$, and $c = 2\Delta_A$ is divided into cells of dimensions $\Delta x = 48.34$ nm and $\Delta z = 7$ nm. Moreover, the time step is selected as $\Delta t = 0.022$ fs to enable compliance with the Courant-Friedrichs-Lewy criterion (2.27). Calculations are made for $\lambda_c \in \{500, 600, 700\}$ nm.

The phenomenon under investigation is illustrated by the spatiotemporal variation of the axial (i.e., x-directed) component of the Poynting vector

$$\mathbf{P}(x, z, t) = \mathbf{E}(x, z, t) \times \mathbf{H}(x, z, t) \tag{2.32}$$

as well as by the three snapshots of the z-directed component of the electric field in Fig.2.2, for $\lambda_c = 600$ nm and $d = \lambda_c$. The pulse-modulated SPP wave is launched at $t = 0$ from the plane $x = -a$. The snapshots of $E_z(x, z, t)$ taken at $t \in \{46.88, 103.64, 184.16\}$ fs are shown in Fig.2.2. The transmitted pulse can be clearly seen in the first snapshot ($t = 46.88$ fs). Thereafter, the signal encounters the right boundary of $\Re_B^{left}$. The signal is partly reflected and partly enters the gap to encounter the left boundary of $\Re_B^{right}$. The second snapshot ($t = 103.64$ fs) clearly shows the reflected signal and the signal in the gap. The third snapshot ($t = 184.16$ fs) shows the reflected signal as well as the signal received in the space $x > d/2$. The received signal consists of a precursor and the main pulse.

The precursor begins to form before the pulse-modulated SPP wave has arrived at the abrupt termination $x = -d/2$ of the metal. The Sommerfeld and Brillouin precursors are formed during the propagation of a pulse-modulated plane wave in a homogeneous dielectric medium, the frequency-dependence of the relative permittivity being responsible for precursor formation [Oughstun and Sherman (1994)]. For a pulse-modulated SPP wave propagating guided by an air/metal interface, the frequency-dependence of the relative permittivity of the metal has to be responsible for precursor formation because air has been assumed to be nondispersive in our calculations.

In order to evaluate the transmission of a pulse carried by an SPP wave across the gap $\mathfrak{R}_A^{bot}$ between $\mathfrak{R}_B^{left}$ and $\mathfrak{R}_B^{right}$, attention is focused on the transmission point R and the reception point S identified in Fig. 2.1. At both of these points, the temporal variation of $\mathbf{P}(x,z,t)$ is determined. In order to separate the signal to be transmitted from the reflected signal received at R, $d_R \geq 25\lambda_c$ is set. The ration $d_S / \lambda_c \in [1, 41]$ is varied with $d = \lambda_c$ fixed. A wide gap in comparison to typical features in semiconductor chips has to be chosen for conservative estimates for the fidelity of information transmission across the gap.
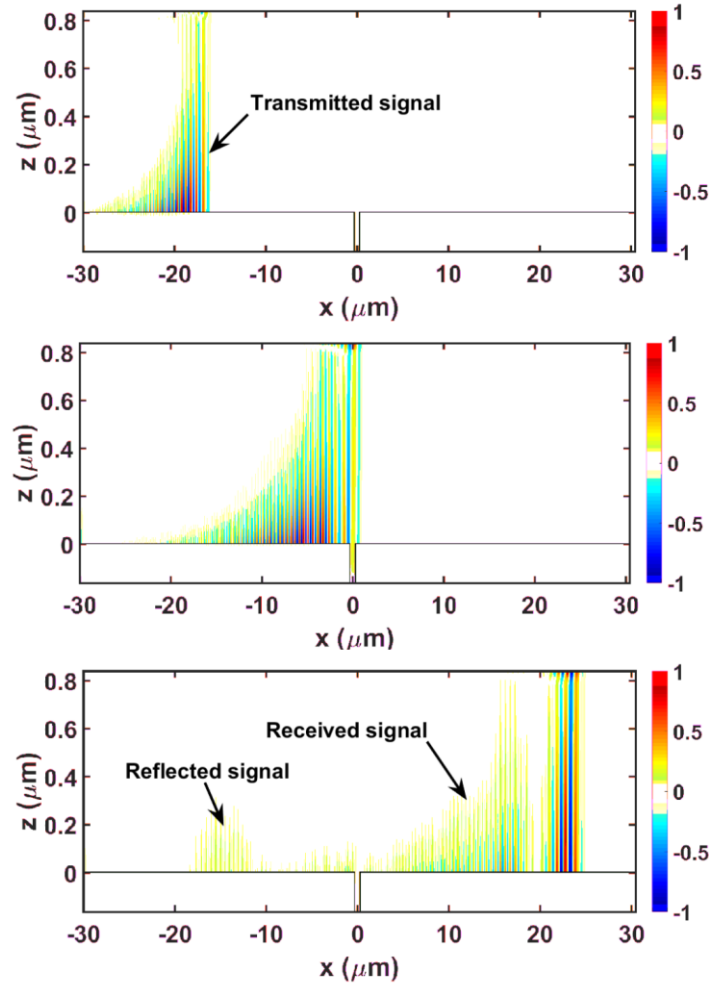
Figure 2.2: Three snapshots of $E_z(x,z,t)$ taken at (top) $t = 46.88$ fs, (middle) $t = 103.64$ fs, and (bottom) $t = 184.16$ fs, when $\lambda_c = 600$ nm and $d = \lambda_c$. $E_z(x,z,t)$ was normalized by 0.084 V m^{-1} in the top snapshot, 0.050 V m^{-1} in the middle snapshot, and 0.039 V m^{-1} in the bottom snapshot.

2.4.1. Launched signal

The signal leaving the plane $x = -a$ propagates through the transmission point R and is then partially launched from the right boundary of $\mathfrak{R}_B^{left}$ into the half-space $x > -d/2$ and partially reflected into the half-space $x < -d/2$. In order to determine the characteristics of the launched signal, we let the region $\mathfrak{R}_B^{right}$ be occupied by material A (instead of material B). In other words, let material B (metal) be terminated abruptly at

the right boundary of $\mathfrak{R}_B^{left}$.

The temporal profile of $P_x(x,z,t)$ at point R is shown in Fig.2.3 when $\lambda_c = 600$

nm for three different value of d_R. Whereas $P_x(x_R, z_R, t)$ for $t \in (0,150]$ fs is shown in

the left column, the same is plotted in the right column for $t \in [150, 250]$ fs. Thus, the left

column shows the transmitted signal and the right column shows the reflected signal at

point R. When $d_R = 35\lambda_c$, the transmitted signal exists for $t \in [29, 90.1]$ fs and the

reflected pulse begins to appear at $t \approx 200$ fs. Similarly, the transmitted signal exists for

$t \in [38.5, 104.1]$ fs and $t \in [48.5, 120.8]$ fs when $d_R = 30\lambda_c$ and $25\lambda_c$, respectively. If the

signal duration is quantified as the time interval for which $P_x(x,z,t)$ exceeds 50% of its

peak value, the signal duration is 10.64 fs for $d_R = 35\lambda_c$, 13.14 fs for $d_R = 30\lambda_c$, and 16.11

fs for $d_R = 25\lambda_c$. The increasing signal duration at R as that point is chosen closer to the

right edge of $\mathfrak{R}_B^{left}$ indicates that the pulse broadens as it propagates on the metal/air

interface. This observation is consistent with different spectral components of the

transmitted signal having different phase speeds because of the ω-dependence of $\tilde{\chi}_B$.

Furthermore, in Fig.2.3, the peak intensity of the pulse at R decreases, the closer

that point is to the right edge of $\mathfrak{R}_B^{left}$. This observation is consistent with attenuation of

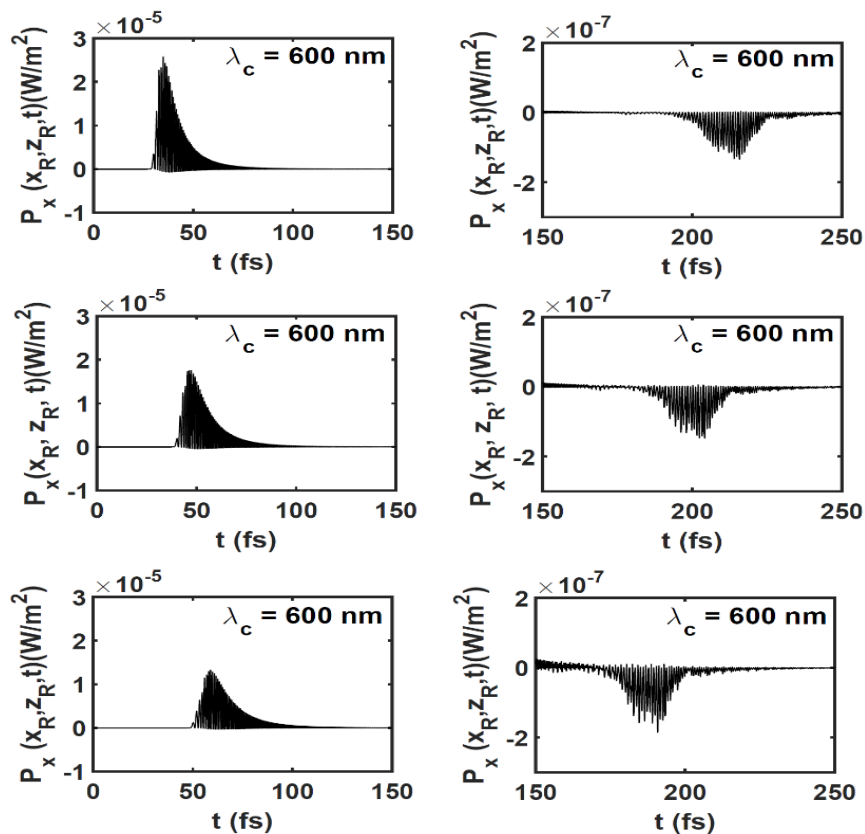the carrier SPP wave because $\mathrm{Im}(q_c) > 0$ as the metal is dissipative.

Figure 2.3: Temporal profile of $P_x(x_R, z_R, t)$ when $\lambda_c = 600$ nm and the region $\mathfrak{R}_B^{right}$ is occupied by material A. (Top) $d_R = 35\lambda_c$, (middle) $d_R = 30\lambda_c$, and (bottom) $d_R = 25\lambda_c$.

The transmitted signal (left) and the reflected signal (right) at point R are sufficiently separated from each other in time to be distinctly identified.

In all three panels of Fig.2.3, the reflected signal is very weak. Therefore, the vast majority of the signal energy leaving the plane $x = -a$ is either dissipated in the metal as the carrier SPP wave propagates along the upper surface of $\mathfrak{R}_B^{left}$ or is transmitted into the half-space $x > -d/2$.

The temporal profile of $P_x(x, z, t)$ at the reception point S is shown in Fig.2.4 for $d_S / \lambda_c \in \{4, 20, 40\}$ when $\lambda_c = 600$ nm and the region $\mathfrak{R}_B^{right}$ is occupied by material A. The received signal has two distinct parts: (i) a precursor followed by (ii) the main pulse with a lower peak intensity. Whereas the precursor does not appear to weaken or significantly deform as S is chosen farther from the right edge of $\mathfrak{R}_B^{left}$, the main pulse

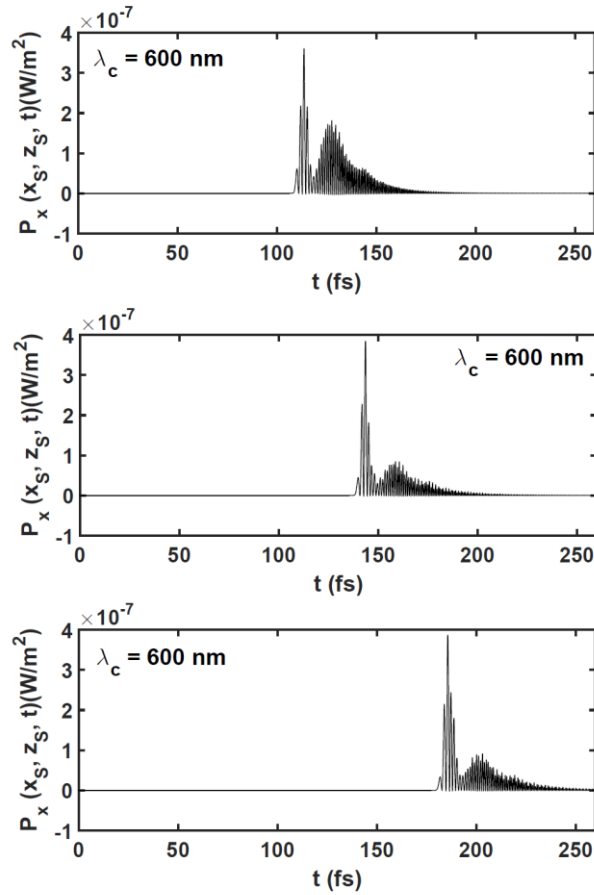initially weakens as the distance d_S increases but then appears to stabilize.

Figure 2.4: Temporal profile of $P_x(x,z,t)$ when $\lambda_c = 600$ nm and the region $\Re_B^{right}$ is occupied by material A. (Top) $d_S = 4\lambda_c$, (middle) $d_S = 20\lambda_c$, and (bottom) $d_S = 40\lambda_c$.

For all three values of d_S in Fig.2.4, the main pulse is a somewhat distorted version of the launched pulse, the distortion being the appearance of a subsidiary peak later in time. Thus, even though the propagation of the SPP carrier wave must end at the right edge of $\Re_B^{left}$ because material B is replaced by material A for $x > -d/2$, information encoded as the existence of a pulse (as in an ON/OFF code) continues to propagate in the forward direction for a long distance. Indeed, the temporal profiles of $P_x(x_S, z_S, t)$ for $d_S = 20\lambda_c$ and $d_S = 40\lambda_c$ are approximately the same. The propagation of the SPP carrier wave after the metal ends is due to both main pulse and precursor field.

In order to quantify the similarity of the signal received at point S to the signal

transmitted at point R, the Pearson correlation coefficient ρ_{RS} [Rodgers and Nicewander (1988)] between the transmitted and received signals is determined. Suppose that both $P_x(x_R, z_R, t)$ and $P_x(x_S, z_S, t)$ are sampled at discrete instants of time t_ℓ, $\ell \in [1, N]$. Then, the Pearson correlation coefficient is defined as

$$\rho_{RS} = \frac{\sum_{\ell=1}^{N} \left[\Delta P_x(x_R, z_R, t_\ell) \cdot \Delta P_x(x_S, z_S, t_\ell - \bar{t}) \right]}{\sqrt{\sum_{\ell=1}^{N} \left[\Delta P_x(x_R, z_R, t_\ell) \right]^2 \cdot \sum_{\ell=1}^{N} \left[\Delta P_x(x_S, z_S, t_\ell - \bar{t}) \right]^2}}, \tag{2.33}$$

where

$$\Delta P_x(x, z, t_\ell) = P_x(x, z, t_\ell) - \frac{1}{N} \sum_{\kappa=1}^{N} P_x(x, z, t_\kappa) \tag{2.34}$$

for $\ell \in [1, N]$ and $\bar{t} = d_{RS} / c_0$ is the time of flight of a plane wave in a air across the distance $d_{RS} = d_R + d + d_S$. Small adjustments to $\bar{t}$ have to be made so that the onsets of the received and the transmitted signals coincide.

The range of ρ_{RS} is [-1, 1]. Positive values of ρ_{RS} indicate a strong correlation, whereas negative values indicate a lack of correlation. The closer that $|\rho_{RS}|$ is to unity, the stronger is the correlation or anticorrelation, as indicated by the sign of ρ_{RS}.

In order to calculate ρ_{RS}, $d_R / \lambda_c = 30$ is fixed but $d_S / \lambda_c \in [1, 41]$ is varied so that $d_{RS} / \lambda_c \in [32, 72]$. The graph of ρ_{RS} as a function of d_{RS} / λ_c for $\lambda_c = 600$ nm is shown in Fig.2.5. The Pearson correlation coefficient ranges from 0.65 to 0.52. Whereas the shapes of the transmitted and received signals are positively correlated, the correlation is not perfect. As d_{RS} / λ_c increases from 32 to 35, ρ_{RS} decreases. But ρ_{RS} is almost constant for $d_{RS} / \lambda_c \in [35, 72]$, which is a very long distance, especially inside a chip. Such high values of ρ_{RS} for large values of d_{RS} augur well for information transmission across the gap $\mathfrak{R}_A^{bot}$ when $\mathfrak{R}_B^{right}$ is indeed occupied by material B, even for d many times larger
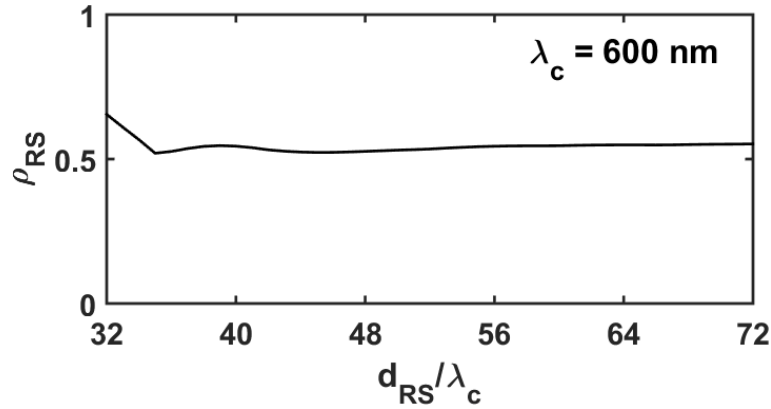
than λ_c.

Figure 2.5: Pearson correlation coefficient between $P_x(x_R, z_R, t)$ and $P_x(x_S, z_S, t)$ as a function of d_{RS} when $d_R = 30\lambda_c$, $\lambda_c = 600$ nm, and the region $\mathfrak{R}_B^{right}$ is occupied by material A.

2.4.2. Transmission Across a Gap

Let the gap be restored by having R_B^{right} occupied by material B. Thus, the region $\mathfrak{R}_B = \mathfrak{R}_B^{left} \cup \mathfrak{R}_B^{right}$ is now totally occupied by material B and the width of the gap occupied by material A is finite.

The temporal profiles of $P_x(x_R, z_R, t)$ for $d_R = 30\lambda_c$ are shown in Fig.2.6 for $\lambda_c \in \{500, 600, 700\}$ nm. The profile for $\lambda_c = 600$ nm agrees with the one in Fig.2.3, the reflected pulse is very weak. The same is true for $\lambda_c \in \{500, 700\}$ nm.

A comparison of the three profiles in Fig.2.6 reveals that the peak intensity of the transmitted signal increases as λ_c increases. This observation is consistent with the variation of q_c with λ_c, as depicted in Fig.2.7. The attenuation rate quantitated via $\text{Im}(q_c)$ decreases as λ_c increases. Plots in the right column of Fig.2.6 show that (i) the reflected signal is about a hundred times weaker than the transmitted signal and (ii) the reflection is weaker if the carrier wavelength is higher.
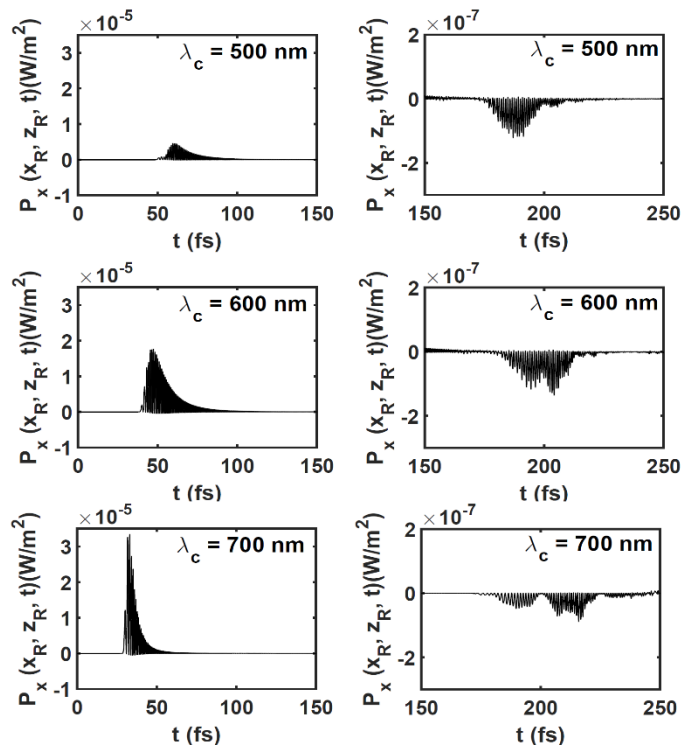
Figure 2.6: Temporal profile of $P_x(x_R, z_R, t)$ when $d_R = 30\lambda_c$ and the region $\mathfrak{R}_B^{right}$ is occupied by material B. (Top) $\lambda_c = 500$ nm, (middle) $\lambda_c = 600$ nm, and (bottom) $\lambda_c = 700$ nm. The transmitted signal (left) and the reflected signal (right) at point R are sufficiently separated from each other in time to be distinctly identified.
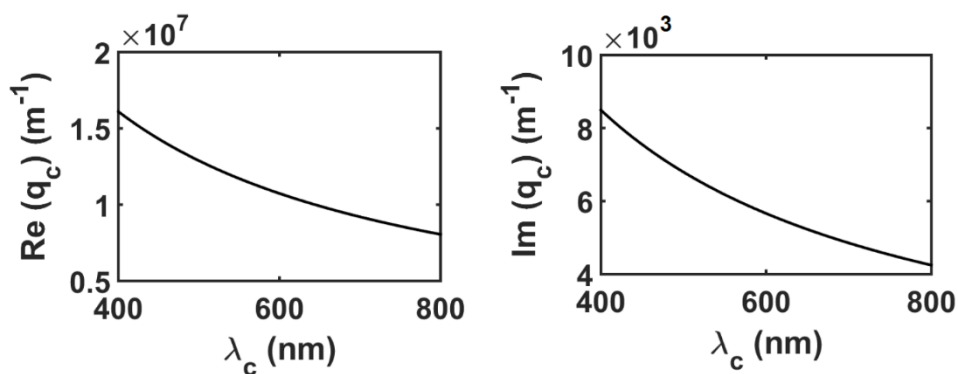

Figure 2.7: Real and imaginary part of q_c versus $\lambda_c \in [400, 800]$ nm.

Furthermore, the transmitted signal's duration is markedly lower for $\lambda_c = 700$ nm than for the other two values of λ_c. Quantified as the time interval for which $P_x(x, z, t)$ exceeds 50% of its peak value, the signal duration is 14.65 fs for $\lambda_c = 500$ nm, 13.14 fs

for $\lambda_c = 600$ nm, and 5.2 fs for $\lambda_c = 700$ nm. This means that the spectrum of the signal

at R has a larger bandwidth when λ_c is higher. Indeed, as shown by the spectra of

$P_x(x_R, z_R, t)$ plotted in Fig.2.8, the full-width-at-half-maximum (FWHM) bandwidth is

464.2 THz for $\lambda_c = 500$ nm (i.e., $f_c = 600$ THz), 705.6 THz for $\lambda_c = 600$ nm (i.e.,

$f_c = 500$ THz), and 724.2 THz for $\lambda_c = 700$ nm (i.e., $f_c = 428.6$ THz). Note here

parenthetically that the peak frequency of the spectrum of the Poynting vector in Fig.2.8.

is twice the peak frequency of the electric or magnetic field.

Figure 2.9 provides temporal profiles of $P_x(x_S, z_S, t)$ for $d_{RS} / \lambda_c \in \{35, 50, 70\}$

and $\lambda_c \in \{500, 600, 700\}$ nm, with $d_R / \lambda_c = 30$. Just as in Fig. 2.4, each panel in Fig.2.9

indicates that signal received at S comprises a precursor followed by the main pulse. In

seven of the nine panels in the figure, the precursor's peak is significantly higher than the

peak of the main pulse; in the remaining two panels, the two peaks are of comparable

magnitudes. The main received pulse appears to be a distorted version of the transmitted

pulse (Fig.2.6), the distortion depending on the carrier wavelength λ_c and therefore being

affected by the dispersion characteristics of the carrier SPP wave illustrated in Fig. 2.7.

Examination of any column of Fig. 2.9 reveals that the signal is received after a

greater delay as the distance d_{RS} between the transmission and reception points increases,

in accord with a finite maximum signal speed [Maksimenko et $al.$ (1997)]. Examination

of any row of the same figure shows that the peak intensity of the received signal increases

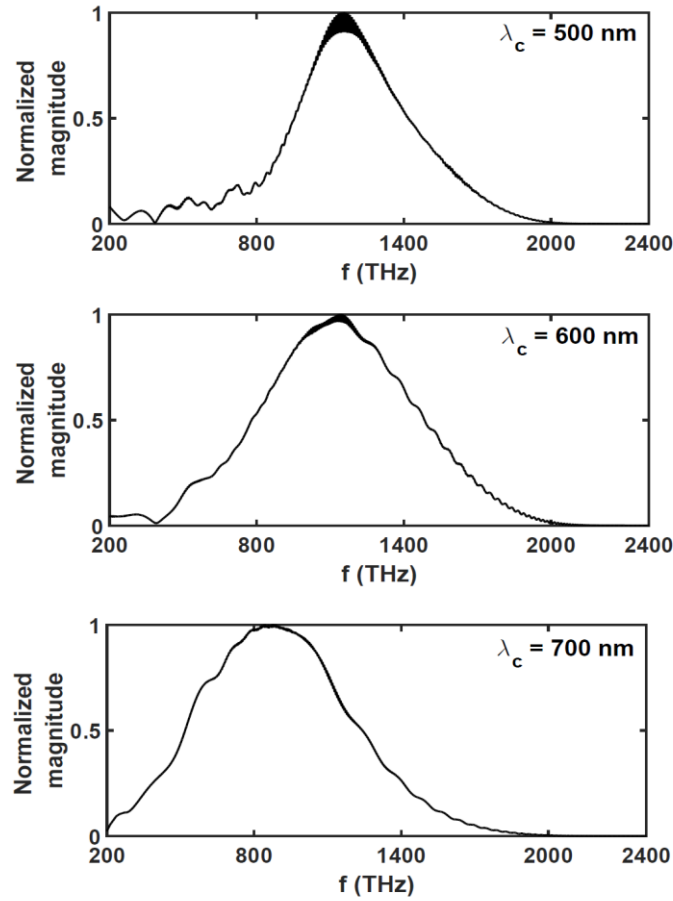as λ_c increases, consistently with the variation of $\mathrm{Im}(q_c)$ with λ_c depicted in Fig. 2.7.

Figure 2.8: Normalized spectra of $P_x(x_R, z_R, t)$ when $d_R = 30\lambda_c$ and the region $\mathfrak{R}_B^{right}$ is occupied by material B. (Top) $\lambda_c = 500$ nm (i.e., $f_c = 600$ THz), (middle) $\lambda_c = 600$ nm (i.e., $f_c = 500$ THz), and (bottom) $\lambda_c = 700$ nm (i.e., $f_c = 428.6$ THz).

The precursor is less separated from the main pulse in Fig. 2.9 as λ_c increases; indeed, for $\lambda_c = 700$ nm the two components of the received signal coalesce together rather well. That coalescence implies that the signal received at S is correlated well with the signal transmitted at R.

Figure 2.10 shows the variation of ρ_{RS} with d_{RS} for $\lambda_c \in \{500, 600, 700\}$ nm, when $d_R = 30\lambda_c$. For any of the three carrier wavelengths, ρ_{RS} stabilizes to a constant value beyond some threshold value of d_{RS}.

Thus, for $\lambda_c = 500$ nm, ρ_{RS} first decreases from 0.62 at $d_{RS}/\lambda_c = 32$ to 0.47 at

$d_{RS} / \lambda_c = 40$ and then remains virtually constant at 0.50 as d_{RS} increases to 72. As

d_{RS} / λ_c increases from 32 to 40, the energy content of the main pulse decreases and that

of the precursor increases, but the former exceeds the latter. Beyond $d_{RS} / \lambda_c = 40$,

however, the energy of the precursor is large compared to that of the main pulse. The

same trends are observed for $\lambda_c = 600$ nm: ρ_{RS} first decreases from 0.70 at $d_{RS} / \lambda_c = 32$

to 0.46 at $d_{RS} / \lambda_c = 44$ and then remaining virtually constant at 0.53 regardless of the

increase in the value of d_{RS}. For $\lambda_c = 700$ nm, ρ_{RS} first increases from 0.60 at

$d_{RS} / \lambda_c = 32$ to 0.68 at $d_{RS} / \lambda_c = 50$ and then stabilizes at 0.70 as d_{RS} increases to 72. A

drop in the Pearson correlation coefficient for $\lambda_c = 700$ nm does not occur because the

precursor and the main pulse are not as widely separated as for $\lambda_c \in \{500, 600\}$ nm; see
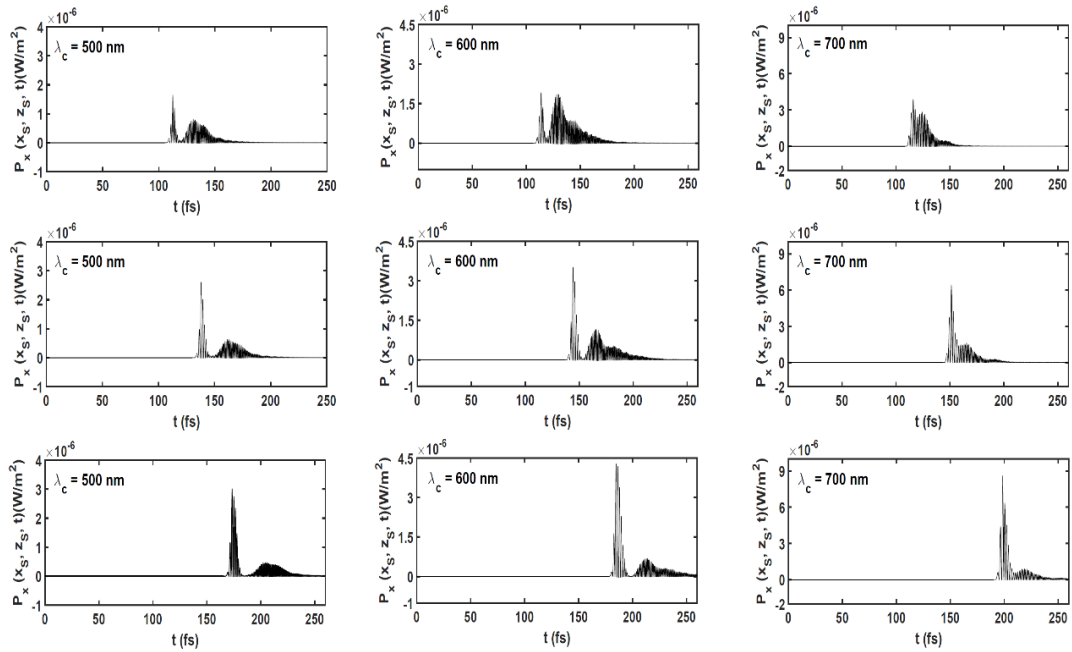
Fig. 2.9.

Figure 2.9: Temporal profile of $P_x(x_S, z_S, t)$ when $d_R / \lambda_c = 30$ and the region $\mathfrak{R}_B^{right}$ is

occupied by material B. Top row: $d_{RS} = 35\lambda_c$, middle row: $d_{RS} = 50\lambda_c$, and bottom row:

$d_{RS} = 70\lambda_c$. Left column: $\lambda_c = 500$ nm, middle column: $\lambda_c = 600$ nm, and right column:
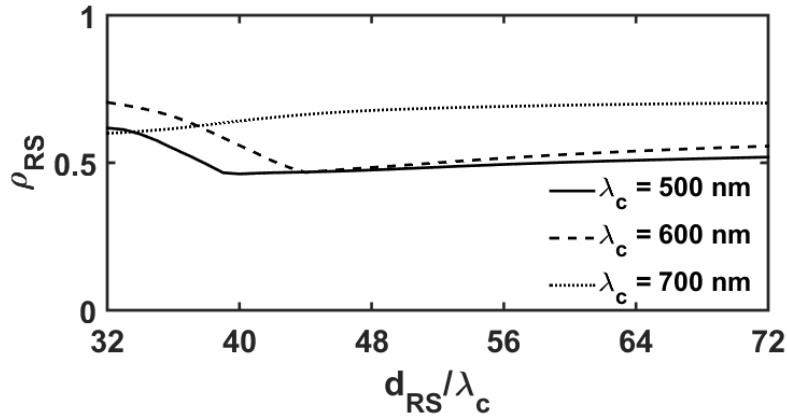
$\lambda_c = 700$ nm.

Figure 2.10: Pearson correlation coefficient between $P_x(x_R, z_R, t)$ and $P_x(x_S, z_S, t)$ as a function of d_{RS} when $d_R = 30\lambda_c$, $\lambda_c \in \{500, 600, 700\}$ nm, and the region $\Re_B^{right}$ is occupied by material B.

The stabilization of ρ_{RS} at a higher value when λ_c is higher is in accord with the frequency dependence of $\tilde{\chi}_B$. The farther away that λ_c is from the absorption band of the metal (here, silver), the lesser is the attenuation rate of the carrier SPP wave (Fig. 2.7) and the lesser is the degree of pulse broadening. The stabilization of the PCC beyond a threshold value of d_{RS} bodes well for surface-plasmonic communication inside a chip.

When $\lambda_c = 600$ nm, the precursor and the main pulse in the signal received at S are very close for $d_S = 0$ but the two are far apart from each other for $d_S = 49\lambda_c$, as shown in Fig. 2.11. Figure 2.11 also shows the spectra of $P_x(x_S, z_S, t)$ for $\lambda_c = 600$ nm and $d_S / \lambda_c \in \{0, 49\}$. These spectra are very different from the spectrum of the transmitted signal in Fig. 2.8 (middle), because the transmitted signal at R is just a pulse. The transmitted signal's peak frequency is 1139 THz and the full-width-at-half-maximum (FWHM) bandwidth is 705.6 THz.

When the precursor is very close to the main pulse, the total energy of the former is much smaller in comparison to the total energy of the latter, as shown in the top left panel of Fig. 2.11. This is confirmed by the spectra of the precursor (peak frequency 586.4

62

THz, FWHM bandwidth 206 THz) and the main pulse (peak frequency 1037 THz, FWHM bandwidth 250.2 THz) in the top right panel of the same figure. In contrast, the precursor's total energy considerably exceeds that of the main pulse when the precursor is widely separated with the main pulse, as shown in the bottom left panel of Fig. 2.11. Confirmation is provided in the bottom right panel of the same figure, the peak frequency and the FWHM bandwidth of the precursor being 590.1 THz and 207 THz, respectively, and the corresponding quantities for the main pulse being 1034 THz and 265 THz.
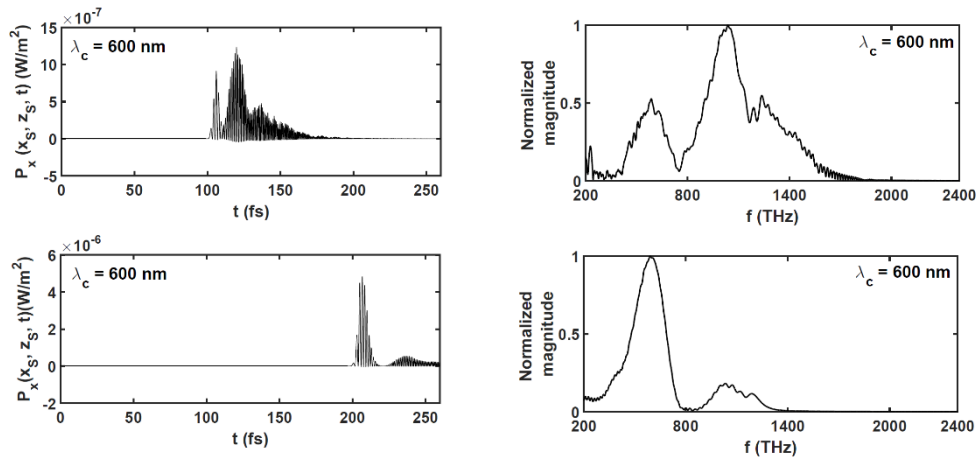

Figure 2.11: $P_x(x_S, z_S, t)$ in the time domain (top left) and frequency domain (top right), when the precursor is very close to the main pulse ($d_S = 0$). Similarly, $P_x(x_S, z_S, t)$ in the time domain (bottom left) and frequency domain (bottom right), when the precursor is widely separated from the main pulse ($d_S = 49\lambda_c$) for $\lambda_c = 600$ nm.

2.5. Concluding Remarks

Numerical simulation of the propagation of a pulse-modulated surface-plasmon-polariton wave guided by the planar interface of metal and air shows that as the signal moves forward, its temporal profile broadens and its amplitude reduces. The broadening is consistent with different spectral components of the signal having different phase speeds, and the amplitude reduction occurs due to the dissipation of electromagnetic energy in the metal.

After an abrupt termination of the metal, reflection is very low and the signal continues to propagate in air. However, beyond the termination, the signal comprises a precursor followed by the main pulse with a lower peak intensity. The main pulse is a somewhat distorted version of the launched pulse, the distortion being the appearance of a subsidiary peak later in time. Although the propagation of the SPP carrier wave must end when the metal ends, information encoded as the existence of a pulse propagates in the forward direction for a long distance. Statistical analysis reveals that the signal after the termination remained strongly and positively correlated with the transmitted signal.

When the metal/air interface is restored after a gap of width equal to the carrier wavelength in free space, the signal received across the gap still comprises a precursor and the main pulse that is still strongly and positively correlated with the transmitted signal. Thus information continues to propagate in the forward direction for a long distance after the gap. The precursor is more separated from the main pulse and the attenuation of the received signal is higher if the carrier SPP wave has a lower free-space wavelength, due to proximity to the absorption band of the metal. These conclusions are promising for SPP-wave-based optical interconnects for faster communication between electronic devices inside a semiconductor chip.